Arab J Geosci (2015) 8:4983–4997
DOI 10.1007/s12517-014-1563-z

ORIGINAL PAPER

Controls on quartzite bearing base-metal sulfide and invisible gold mineralization at Gabal Abu Houdied area, South Eastern Desert, Egypt

W. S. Ibrahim · K. Watanabe · M. E. Ibrahim · K. Yonezu

Received: 30 May 2014 / Accepted: 14 July 2014 / Published online: 26 July 2014
© Saudi Society for Geosciences 2014

Abstract The Neoproterozoic basement rocks cropping out in the Gabal Abu Houdied (GAH) area comprises mainly three lithotectonic assemblages; mafic–ultramafic ophiolitic rocks, island arc-related metasediment–metavolcanic rocks and syn- and post-tectonic intrusions. The base-metal sulfide and invisible gold mineralization are restricted to quartzites, which are considered as member of island arc-related metasediment rocks. The mineralized quartzite rocks are cropped out at three localities, at Wadi El Haussioum where cover a small area (0.25 km^2), at Bir Abu Houdeid, cover small area (0.5 km^2), and at Bir Shani (3.5 km long with different width ranging from 4 to 75 m). Based on textural characteristics and chemical features, documented by electron probe microanalysis (EPMA) and inductively coupled plasma mass spectrometry analyses (ICP-MS), two phases of sulfide minerals assemblages in the investigated quartzites of GAH area. An early mineralization phase includes pyrite, pyrrhotite, argentite (acanthite) and invisible gold, and the late phase, dominated by pyrite, galena, sphalerite, chalcopyrite, covelite, and±invisible gold. Analyses of the structural data collected from the quartzite rocks and surroundings indicated that the base-metal sulfide and associated gold mineralization in the GAH area are mostly controlled by D3 transperssional deformation event. This event is main Hamisana shear zone (HSZ) deformation event and characterized by transperssional stress regime, with σ1 trending E–W and σ3 trending N–S governed conjugate NNW sinistral and NNE–SSW dextral strike slip faulting.

W. S. Ibrahim · K. Watanabe · K. Yonezu
Department of Earth Resources Engineering, Faculty of Engineering, Kyushu University, Fukuoka 819-0395, Japan

W. S. Ibrahim (✉) · M. E. Ibrahim
Nuclear Materials Authority, Cairo, Egypt
e-mail: W-Ibrahim@mine.kyushu-u.ac.jp

Keywords Gabal Abu Houdied · Hamisana · Pyrite · Invisible gold

Introduction

The Arabian–Nubian Shield (ANS) is a famous model of an accretionary orogen with numerous terranes and suture zones (Kröner et al. 1987; Stern 1994; Abdelsalam and Stern 1996; Abdelsalam et al. 2003). The sutures, typically reactivated as transpressional/transcurrent zones, are located across the shield (Johnson and Woldehaimanot 2003). Late deformation included the occurrence of lateral escape tectonics along transtensional or transpressional systems during the final stages of orogeny (Burke and Sengör 1986; Stern et al. 1989; Kröner et al. 1992; Miller and Dixon 1992; Stern 1994; de Wall et al. 2001; Johnson et al. 2011). The distribution of gold as well as base-metal sulfide occurrences in the Eastern Desert of Egypt is controlled by major wrench faults and shear zones (Loizenbauer and Neumayr 1996; Helmy et al. 2004; Zoheir 2008a, b, c; Zoheir 2011). Gold deposits across the southern part of the Eastern Desert are mostly related to NW- or NNW-striking shear zones generally reflecting reactivated earlier accretionary suture zones (Kusky and Ramadan 2002; Zoheir 2008a,b, 2011).

The Gabal Abu Houdeid (GAH) area is located at the southern part of the Eastern Desert of Egypt, at the boundaries between Egypt and Sudan. It is considered as the extreme northern portion of the Hamisana shear zone (HSZ) (Fig. 1a). The HSZ is one of the major high strain zones of the Pan-African (Neoproterozoic) ANS. It trends broadly N–S from northern Sudan into southeastern Egypt and meets the present Red Sea coast at 23° N (de Wall et al. 2001). The base-metal sulfide and invisible gold mineralization at GAH area are restricted to quartzite rocks, which considered as member of island arc-related metasediment rocks. The mineralized

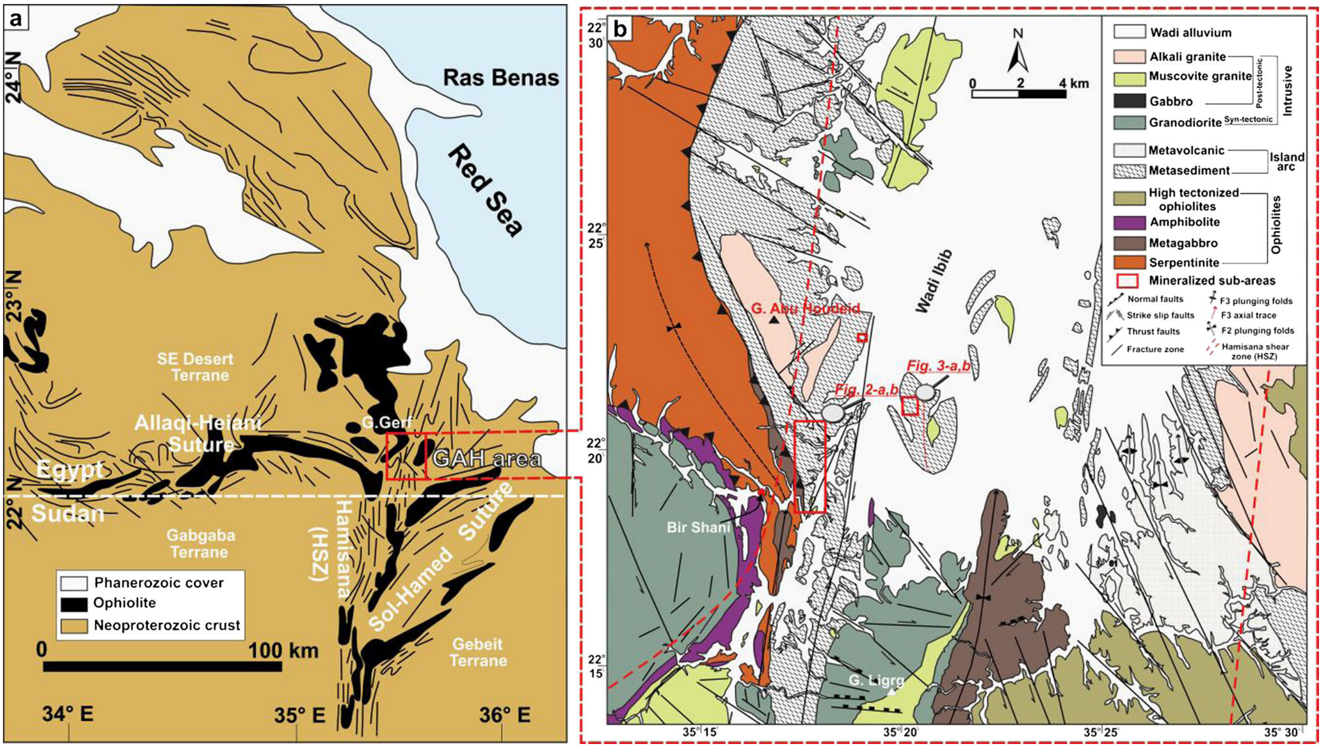

Fig. 1 **a** Location of the study area (modified after Abdelsalam et al. 2003), showing the N-trending Hamisana zone, cutting Neoproterozoic rocks in south Egypt and north Sudan. **b** Geological and structural map of the GAH area and surroundings

quartzite rocks are cropped out at three localities in the investigated area, at Wadi El Haussioum where cover a small area (0.25 km^2), at Bir Abu Houdeid, cover as small area (0.5 km^2), and at Bir Shani, it covers a relatively larger area (3.5 km long with different width ranging from 4 to 75 m).

The present study addresses and investigates the interrelationship between the base-metal sulfide and invisible gold mineralization and tectonic setting of Gabal Abu Houdied (GAH), which discovered by the Egyptian Nuclear Materials Authority (NMA) exploration project, the author is a member in this project. There are no other published literatures on this mineralization at GAH area. In this communication, we first briefly describe the detailed geology of the study area, with emphasis on base-metal sulfide and gold mineralization, followed by results of detailed EPMA, and ICP-MS analyses of various generations of pyrite from the ore zone. Another important contribution of this study relates to anomalously high concentrations of invisible gold in pyrite.

Materials and methods

High-resolution mapping of the lithotectonic units, and major structures in the study area was supported by using false color composite and band ratio satellite images (ASTER) interpretation. Detailed topographic and geologic maps for the mineralized quartzites were constructed on the base of a grid pattern 25×25 m. Fieldwork involved sampling of the mineralized quartzites, structural measurements, and lithological identification.

Petrographic and ore microscopy studies are done on 45 thin and polished sections of mineralized quartzites. Twenty of these polished sections were chosen for EMPA (EPMA-1600 Shimadzu) at Kyushu University (Japan). Twenty representative quartzite samples were chosen for geochemical studies. The major and trace elements analyses were done at department of Earth Resources Engineering, Kyushu University (Japan) using Rigaka X-ray Fluorescence spectrometer 3100. Nineteen pyrite samples have been separated from quartzite host rocks by using heavy liquid separation method for trace elements in pyrite using ICP-MS at Kyushu University (Japan). Five pyrite samples hand-picked from powdered mineralized quartzites were examined for sulfur isotope compositions at Stable isotope Laboratory, the Scottish Universities Environmental Research Centre (UK). The standard technique described by Robinson and Kussakabe (1975) was used in order to determine sulfur isotope. This tool characterized as SO_2 gas was liberated by burning the sulfides with excess Cu_2O at 1,075 ° C, in vacuum. Liberated gases were analyzed on VG Isotech SIRA II mass spectrometer, and standard corrections utilized to raw $\delta^{66}SO_2$ values to yield true $\delta^{34}S$.

Geological setting

The Neoproterozoic basement rocks cropping out in the GAH area comprise three lithotectonic units; mafic–ultramafic ophiolitic rocks, island arc-related metasediment–metavolcanic rock assemblages, syn- and post-tectonic intrusions (Fig. 2b). The following is a description based on field observations for each lithotectonic units.

Ophiolitic assemblage

Ophiolitic rocks occur as a structurally complex elongate N–S trending belt in the western and southern part of the GAH. This rock assemblage is represented by serpentinite, metagabbros, amphibolite, and highly tectonized ophiolitic units (Fig. 2b). The serpentinites investigated in the Bir Shani area are serpentinites with meta-peridotite relics and talc-carbonate rocks along the thrust zone between the

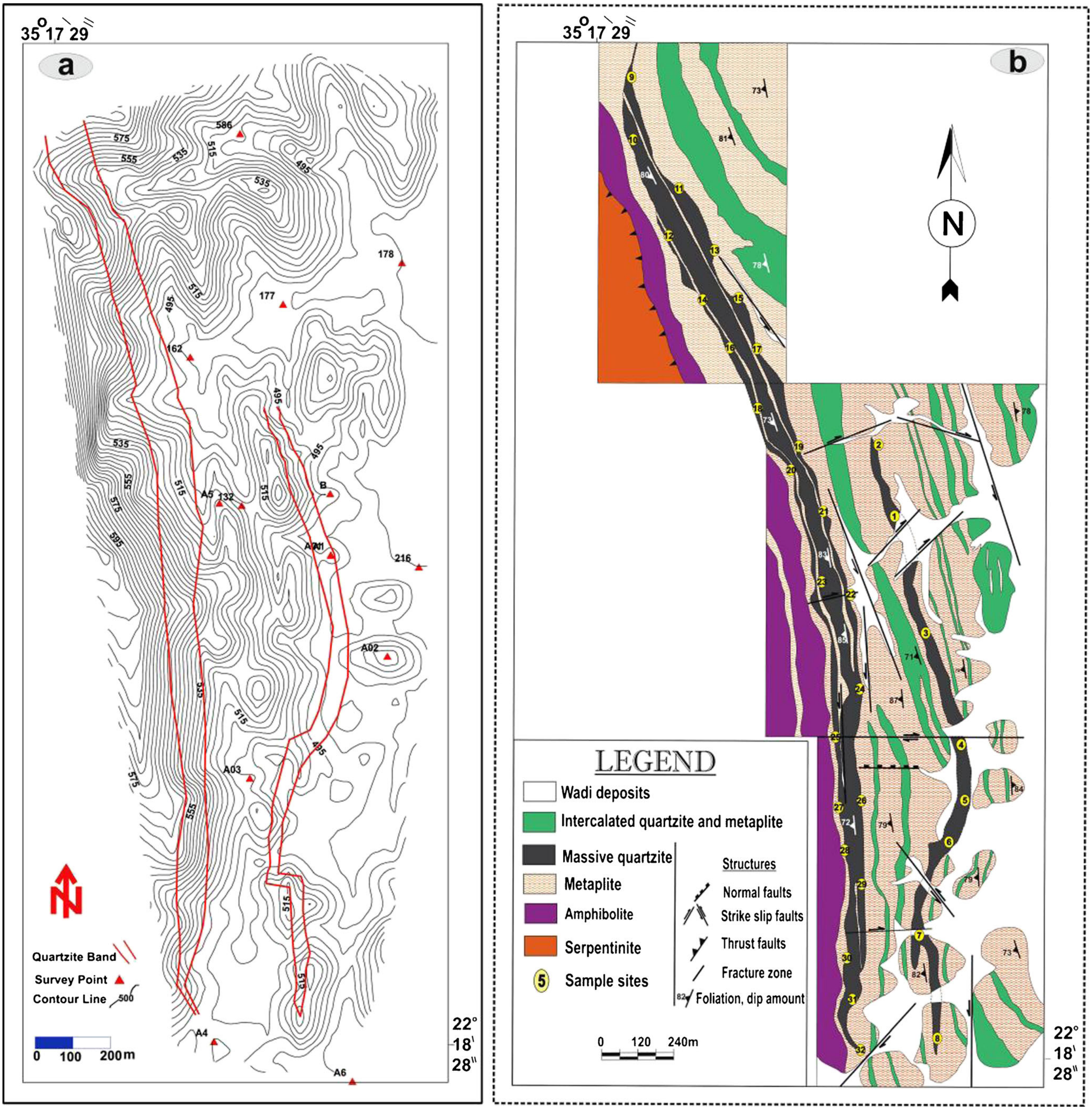

Fig. 2 **a** Topographic contour map of Bir Shani subarea. **b** Detailed geologic map for the quartzite rocks at Bir Shani

serpentinites and other ophiolitic members. These rocks are tectonically thrusted over the metagabbros, amphibolites, and metasediments with low angle thrust contacts. The metagabbros are exposed in the southern part of the study area, east of Bir Shani, often thrust over the metavolcanics, which are in turn overthrusted by serpentinites. The amphibolite rocks expose only in limited locations in the western part of the study area; south of the Geble Abu Houdied and near to Bir Shani. They occur as voluminous thrust-bounded sheets in association with the serpentinite.

Island arc assemblage

The island arc-related assemblage consists of metasediments and metavolcanics. Rocks of this assemblage are intensely deformed and form the footwall of the major thrusts in the western part of the study area (Fig. 2b). The metasediments form a low to moderate topography, and their lithology consist mainly of biotite schists and quartzite bands which are responsible for the mineralization in GAH area. At the northwest end of Wadi Ibib, the metasediments are represented by a NNW–SSE trending belt of strongly foliated, folded, and sheared rock units forming the core of HSZ. The metavolcanics are represented mainly by metabasalt, which display variable degrees of schistosity. These rocks are exposed mainly in the western and southern parts of the study area, forming N–S trending belt in the core of HSZ.

Intrusive assemblage

The intrusive rocks are represented by two main categories including syntectonic intrusions, mainly granitoids and post-tectonic intrusions that include gabbro, muscovite granite and alkali feldspar granites. The syntectonic granites are coarse-grained, enriched in mafic minerals, and are mainly granodioritic in composition. They occur mostly as scattered low-land cones, but they also occur as sharp ridges oriented N–S, especially within the trace of HSZ. Structural investigations revealed that steep to sub-vertical intrusive contacts delimit these plutons, suggesting that magma injection took place along the preexisting structures including foliation planes related to the HSZ deformation event (D3). The post-tectonic intrusions display no foliation and intrude the metasediments, metavolcanics, and ophiolitic rocks. They are distributed over the entire study area; with the gabbros and alkali feldspar granites commonly occurring as small exposures.

Detailed geology of the mineralized subareas

The base-metal sulfide and invisible gold mineralization are restricted to quartzite rocks, which considered as member of island arc-related metasediment rocks. The mineralized quartzite rocks croup out at three localities (Fig. 1b), at Wadi El Haussioum where cover a small area (0.25 km^2), at Bir Abu Houdeid, cover as small area (0.5 km^2), and at Bir Shani, it covers a relatively larger area (3.5 km long different width ranging from 4 to 75 m). Detailed topographic and geologic maps for the mineralized quartzite rocks at Bir Shani and Bir Abu Houdied were constructed on the base of a grid pattern 25×25 m (Figs. 2a and 3a). At Bir Shani, these rocks cover a relatively larger area (3.5 km long with different width ranging from 4 to 75 m) with low to medium peaks almost oriented around N–S trend (Fig. 2b). However, at Bir Abu Houdeid,

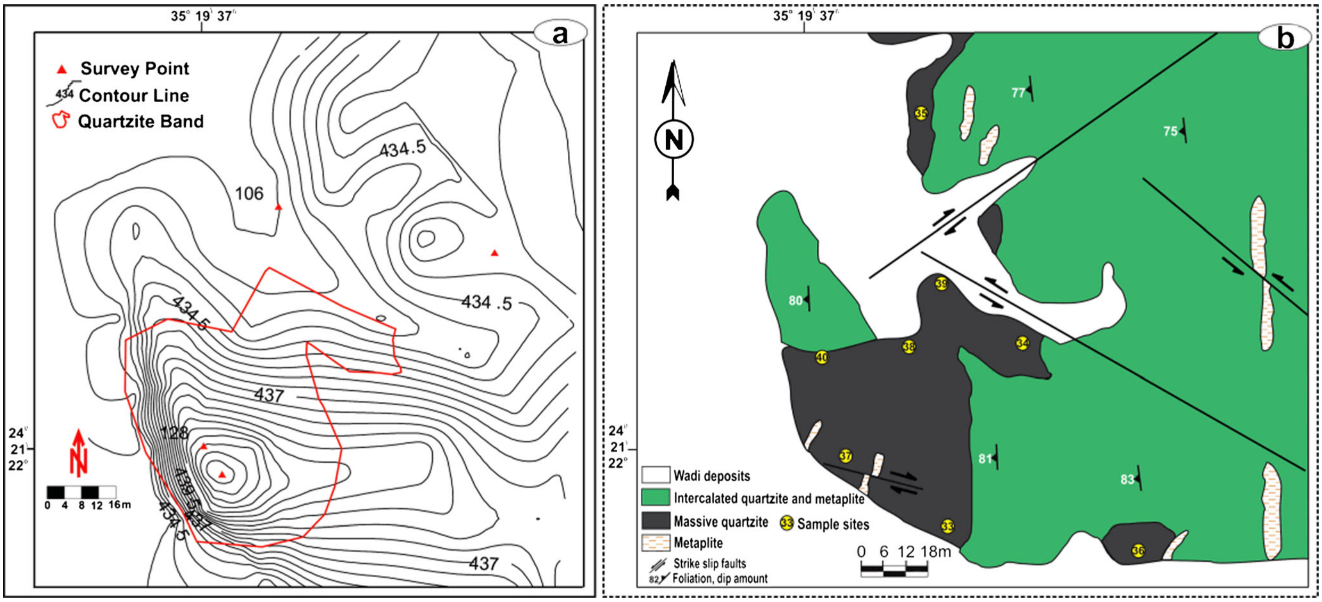

Fig. 3 **a** Topographic contour map of Bir Abu Houdied subarea. **b** Detailed geologic map for the quartzite rocks at Bir Abu Houdied

the quartzite rocks cover small area (0.5 km^2), forming low land terrain (515 m above sea level). They have irregular outcrops highly altered and intercalated with layered metaplite rocks (Fig. 3d).

The quartzite rocks at Bir Shani are intercalated with layered metapelite and highly sheared quartzites and are overlain by altered ultramafic rocks (serpentinite, and amphibolite). These rocks are characterized by sharp contact with the layered metapelite and form higher relief ridges as they are of higher resistance to erosion (Fig. 4a–b). The quartzite rocks are fine to medium grained and white light grey to reddish color (Fig. 4c–d), and usually occur in subparallel striking N 10° W with dip average 70° SW. These rocks are mainly composed of tightly quartz, plagioclase, microcline and opaques with minor muscovite, kyanite, sillimanite, and saturolite are found as accessories. Quartz occurs as subangular to subrounded grains (up to 6 mm) showing wavy extinction (Fig. 5a) with phenocrysts of plate-like and prismatic crystals as well as minute crystals in the groundmass. Sometimes, quartz grains are cracked and frequently showing narrow overgrowth of secondary quartz, also a veinlet of quartz sometimes presents. Plagioclase occurs as subangular grains (up to 2 mm) sometimes with albite twinning (Fig. 5b). Sillimanite occurs as dark elongated fibrous crystals, the sillimanite needless are aligned parallel to subparalleled orientation (Fig. 5c), due to N–S folding related to the third deformational event (D3). Kyanite crystals are seen in samples as fine to medium grained, subhedral with short bladed to prismatic form. Kyanite occurs interstitially between the other minerals in the matrix and rarely as microphenocrysts (Fig. 5a). Muscovite forms thin flakes commonly associated with chlorite which is oriented parallel to the foliation. These

Fig. 4 Field photographs of quartzite rocks exposed in Bir Shani sub-area (**a**–**b**) sharp contact between quartzite (*Qz*) and metapelite (*Mp*) with ridges oriented N–S. **c**–**d** quartzite outcrops with highly hematization

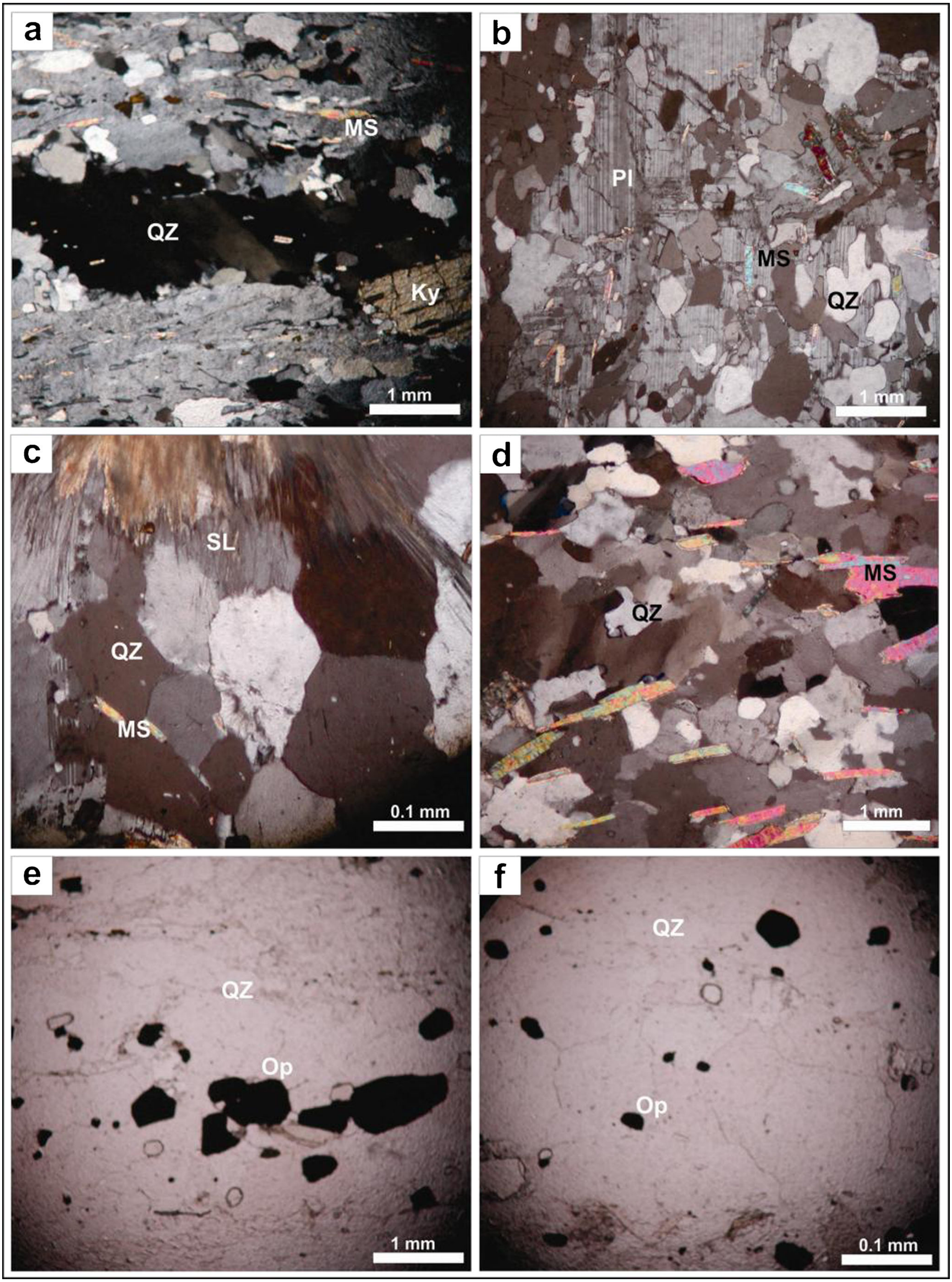
a
MS
QZ
Ky
1 mm
b
Pl
MS
QZ
1 mm
c
SL
QZ
MS
0.1 mm
d
MS
QZ
1 mm
e
QZ
Op
1 mm
f
QZ
Op
0.1 mm

◀ **Fig. 5** Photomicrographs of the quartzite rocks exposed in the GAH area. Abbreviations: *Qz* quartz, *MS* muscovite, *Pl* plagioclase, *Ky* kyanite, *SL* sillimanite, *Op* opaques. **a** Elongate blocky texture in a quartzite with intensively recrystallized quartz porphyroclasts and kyanite; **b** strongly deformed, quartzite with muscovite flakes parallel to the foliation planes; **c** sillimanite needles in quartzite rocks; **d** strongly deformed plagioclase porphyroclasts with intensively recrystallized quartz; **e** rod-like aggregates of opaques manly pyrite (*PPL view*), parallel to the main strike trend (N–S); **f** disseminated opaques manly pyrite (*PPL view*)

flakes show high interference colors with subhedral boundaries (Fig. 5d). The opaque minerals are the most abundant as accessories of the quartzites include sulfide minerals such as pyrite characterized by its black color in PPL view. It occurs in the form of augen—shaped and rod—like large subhedral to anhedral aggregates in parallel to sub parallel manner (Fig. 5e). Also occurs as irregular aggregates of random distribution and in the form of disseminated small grains and skeletal aggregates usually together with quartz (Fig. 5f). It is occasionally reduced along its margins to pyrrhotite. In some samples, the reduction is more advanced to the extent that the pyrite crystals are completely transformed to pyrrhotite.

Structural setting and tectonic evolution

According to structural analysis, field observations and satellite images interpretation, which reveal four deformational events can be distinguished in the Neoproterozic rocks of GAH area. Event D1 a pure compression stress regime with σ1 stress axis trending N–S represents an early shortening event. The N–S compressional regime is in charge of early E–W thrusting and E–W folding (F1) that affected the ophiolitic and island arc-related metasediments. Event D2 characterized by structures developed under ENE–WSW compressional regime (shortening event). This event was recorded in both ophiolitic and island-arc rock assemblages characterized by an association of NW–SE thrust faults and NW–SE (F2) folding. Event D3 transpressional deformation associated with E–W contraction and N–S extension. It is the main event that controlled the deformation along the 610–550 Ma the Hamisana Shear Zone (HSZ) (Stern et al. 1990; Miller and Dixon 1992; Kusky et al. 2003), during the late stages of the collision between the East and West Gondwana in terms of escape tectonics. The E-W transpressional regime was recorded in ophiolitic, island-arc and late-tectonic intrusive (granodiorite) rock assemblages. The parallelism between the magmatic foliation in the granodiorite, and the N–S (S3) mylonitic foliation related to this event in the HSZ, suggests that the intrusion of the granodiorite is considered to have taken place just before or during this deformation phase. The D4 event is interpreted as a post-orogenic extensional event manifested by E–W dextral strike-slip and dip-slip normal faults striking NNW–SSE to N–S and E–W, which began to occur after the emplacement of post-tectonic granites. This event is interpreted as post-orogenic event related to Red Sea rifting, whereas the dextral sense on the E–W trending strike-slip as well as N–S and E–W normal faults are in agreement with the simple shear tectonic model for the Red Sea rift south of latitude 24° to approximately 20° (Ghebreab 1998).

Results

Geochemistry of the mineralized quartzites

The geochemical data of the quartzites are given in Table 1. The major elements of the analyzed quartzite rocks show a variation in SiO_2 (75.41–88.12 wt%), suggesting that they are super mature sandstones. However, there are some samples which contain relatively high SiO_2 concentrations (92.68–94.8 wt%). The relatively low silica samples are characterized by higher Al_2O_3 (8.94–12.01 wt%) in comparison to the samples which have high SiO_2 (Al_2O_3=1.6–7.82 wt%). In the igneous rocks Al inhabits mostly in feldspars. High concentration of Al_2O_3 in the most of the studied samples is probably due to presence of relatively higher amount of feldspar in their mode which is confirmed petrographically. The analyzed samples show variable SiO_2/Al_2O_3 (7.1–54.8) and K_2O/Na_2O (0.01–0.95) ratios (Table 1), K_2O and Na_2O contents and their ratios (K_2O/Na_2O >1) can be attributed to the relative dominance of K-feldspar. The CaO and Na_2O contents show low concentration which, may be contributed by the plagioclases, also the K_2O content shows moderate values and probably reflects derivation from K-feldspars and micas. TiO_2 values in the analyzed quartzite rocks suggest derivation from the TiO_2 containing opaque and mica minerals, while MnO is almost not detected in all analyzed samples and P_2O_5 does not show any significant variation pattern. The geochemical data show variable degrees of negative correlation for SiO_2 against Al_2O_3 (−0.93), TiO_2 (−0.11), K_2O (−0.37), MgO (−0.46), and Na_2O (−0.61), reflecting a decrease in unstable components (e.g., feldspars and rock fragments) with an increase in mineralogical maturity (Gu et al. 2002). Most of the trace elements of these rocks given in (Table 1) like Rb, Ba, and Sr show negative correlation with SiO_2 (−0.34, −0.42, and −0.41, respectively). This suggests that the clastic detritus was associated with silica-rich source component, and Sr is depleted because the recycling of feldspar with increasing maturity. Transition trace elements (TTE) Cr, Co, Ni, and V in quartzite samples are highly variable, Cr (93–280 ppm avg. 155.49 ppm), Co (1–32 ppm avg. 8.4 ppm), Ni (28–80 ppm

Table 1 Major and trace contents in quartzites

Sample	Q1	Q2	Q3	Q4	Q5	Q6	Q7	Q8	Q9	Q10	Q11	Q12	Q13	Q14	Q17	Q18	Q19	Q21	Q23	Q25
SiO_2	79.63	80.96	80.13	79.09	77.24	81.39	79.91	86.68	84.8	81.82	80.34	88.12	82.6	78.42	86.85	81.45	83.33	82.8	80.24	84.72
TiO_2	0.14	0.41	0.57	0.72	0.17	0.17	0.15	0.47	0.44	0.38	0.59	0.53	0.5	0.16	0.41	0.8	0.49	0.53	0.89	0.71
Al_2O_3	9.38	10.13	10.39	11.16	12.01	9.35	8.94	3.92	5.73	7.72	6.28	2.45	6.6	10.23	5.05	6.65	7.52	7.82	7.12	7.61
FeO	2.49	3.47	3.85	3.1	1.09	2.02	2.79	3.71	2.79	3.29	4.49	4.89	4.93	0.91	2.17	2.95	4.03	2.82	4.62	4.68
MnO	–	–	–	–	–	–	–	–	–	–	–	–	–	–	–	–	–	–	–	–
MgO	0.16	0.16	0.16	0.22	0.17	0.16	0.19	0.15	0.15	0.15	0.15	0.16	0.17	0.19	0.18	0.2	0.17	0.16	0.27	0.14
CaO	0.44	0.34	0.21	0.45	0.59	0.56	0.55	0.02	0.03	0.04	0.09	0.04	0.06	0.51	0.19	0.42	0.11	0.11	0.23	0.01
Na_2O	2.88	1.44	1.61	2.04	4.83	3.13	3.37	1.27	2.39	2.16	2.85	0.38	0.32	4.17	1.2	3.95	1.59	2.02	1.49	1.01
K_2O	2.72	0.21	0.13	0.25	2.05	1.52	2.4	1.13	1.99	1.51	2.18	0.18	0.24	2.24	0.39	0.59	0.28	1.92	1.2	0.01
P_2O_5	0.02	0.06	0.06	0.1	0.04	0.03	0.02	0.02	0.2	0.03	0.03	0.02	0.02	0.02	0.04	0.12	0.03	0.04	0.11	0.04
L.O.I.	1.45	1.18	1.31	0.96	1.11	1.07	0.91	1.7	1.08	2.18	1	2.03	1.56	2.25	2.37	1.83	0.95	0.51	0.62	0.71
S	0.6702	1.5606	1.5587	1.933	0.6943	0.6818	0.7644	0.9299	0.3928	0.708	1.9865	1.1918	2.9826	0.8929	1.1637	1.0238	1.4925	1.2494	3.1998	0.3399
Total%	99.98	99.92	99.98	100.02	99.99	100.08	99.99	100.00	99.99	99.99	99.99	99.99	99.98	99.99	100.01	99.98	99.99	99.98	99.99	99.98
Cl (ppm)	55	15	11	37	205	87	196	26	32	22	17	9	15	294	188	2963	8	53	35	8
V	2	55	47	49	7	10	0	22	13	16	36	25	17	5	44	62	27	70	86	51
Cr	151	120	93	117	191	168	125	175	177	113	178	182	134	179	181	131	94	163	131	126
Co	4	3	0	14	0	10	12	29	16	9	–	17	11	32	–	6	–	4	3	13
Ni	51	34	37	34	62	56	39	51	50	35	55	44	43	49	60	36	32	51	30	39
Cu	29	19	72	27	37	42	7	12	1	18	21	16	2	11	3	2	39	9	25	–
Zn	14	–	–	–	–	–	31	–	–	–	–	–	–	19	–	–	–	–	–	–
Pb	5	–	–	2	3	5	1	–	–	–	1	–	–	3	–	16	–	–	10	–
Au	–	–	–	–	–	–	–	–	–	–	–	–	–	–	–	–	–	–	–	–
Ag	–	1	1	5	6	2	–	1	8	6	3	–	5	7	9	7	6	–	4	–
Hg	2	–	–	–	2	–	–	–	–	1	–	–	–	–	–	1	–	–	2	–
Cd	–	–	–	–	0	–	2	–	–	–	–	–	1	–	–	–	–	–	1	–
As	6	3	5	3	7	7	7	3	5	4	4	2	4	6	3	5	6	5	3	3
Sb	9	8	10	–	11	7	14	5	3	8	12	9	9	11	7	8	10	8	10	10
Sn	9	–	8	–	9	2	8	4	2	4	5	7	7	7	–	7	3	6	3	11
Bi	3	–	–	2	–	2	2	–	2	–	1	–	–	–	–	1	1	2	–	3
Mo	12	3	4	4	14	12	20	5	4	5	7	20	5	12	4	8	10	7	8	4
W	55	27	57	45	33	39	65	35	30	55	53	42	32	46	45	40	46	49	49	57
Rb	15	–	–	1	10	9	10	–	–	1	1	–	–	9	2	–	–	–	9	–
Sr	71	162	106	232	115	111	74	32	42	49	95	44	50	62	167	444	250	46	253	14
Ba	437	77	46	34	276	272	364	9	–	17	–	–	–	222	111	23	82	–	136	–

Table 1 (continued)

Sample	Q1	Q2	Q3	Q4	Q5	Q6	Q7	Q8	Q9	Q10	Q11	Q12	Q13	Q14	Q17	Q18	Q19	Q21	Q23	Q25
Y	56	33	34	68	77	72	48	11	6	10	10	8	10	51	12	30	8	9	25	4
Zr	273	169	168	181	263	257	310	159	106	137	135	142	135	327	135	303	172	159	171	185
Nb	8	5	5	7	8	7	7	4	5	4	4	5	4	8	5	7	5	6	5	6
Th	1	4	1	–	2	2	–	4	1	4	–	–	1	2	4	5	–	1	3	–
U	–	1	1	6	–	–	–	2	1	–	2	1	–	–	2	1	2	2	–	–
SiO_2/Al_2O_3	8.5	8.0	7.7	7.1	6.4	8.7	8.9	22.1	14.8	10.6	12.8	36.0	12.5	7.7	17.2	12.2	11.1	10.6	11.3	11.1
K_2O/Na_2O	0.94	0.15	0.08	0.12	0.42	0.49	0.71	0.89	0.83	0.70	0.76	0.47	0.75	0.54	0.33	0.15	0.18	0.95	0.81	0.01

"–" below detection limit

avg. 46.63 ppm), and V (2–87 ppm, avg. 31.91 ppm) (Table 1). A strong positive correlation of Cr with Ni (0.82) in these rocks indicates that control of the quartzites by surrounding mafic/ultramafic rocks, which provided additional inputs during the sedimentation processes.

Ore mineralogy and paragenesis

According to ore petrography and geochemical studies of the quartzites, the base-metal sulfide minerals represent around 10 % of volume of these rocks. studying the textures (overgrowth, inclusions, and replacement) and the data obtained from the microanalyses (SEM-EDX and EPMA) in the mineralized quartzites suggests the presence of at least two phases of sulfide minerals assemblages in the investigated quartzites of GAH area. The early mineralization phase includes pyrite, pyrrhotite, argentite, and invisible gold. This phase occurs commonly as augen—shaped and rod—like aggregates in parallel to sub parallel manner (Fig. 6a, b). On the other hand, the late phase, dominated by pyrite, galena, sphalerite, chalcopyrite, covellite, and±invisible gold, is occurring as disseminated fine prismatic grains or overgrowths on the former (early phase) pyrite and grains. The ore microscopic observations of several polished sections indicated that, pyrite, pyrrhotite, argentite, galena, sphalerite, chalcopyrite, and covelite are the main base-metal sulfide minerals associated with gold mineralization. Pyrite is the most abundant ore mineral (>60 vol% of sulfide minerals) in the quartzites. In the early phase, it occurs mainly as large subhedral to anhedral aggregates, up to 5 mm in size, identifiable ductile–brittle deformation textures in this pyrite generation are widespread, commonly in zones of high bulk strain within HSZ. Dislocation microstructures in the early pyrite are characterized by straight to slightly curved and/or stepped. Preferred grain shape orientation in this pyrite phase (Fig. 6a–c) occurs in areas of high bulk strain in which thin, discontinuous, often anastomosing zones define the foliation related to third deformational event (D3). Silver (argentite) is less common sulfide mineral in this stage, it is observed as inclusion in pyrite grains (Fig. 6d).

On the other hand, pyrite of the late sulfide stage occurs as disseminated small grains (<300 μm), commonly associated with other sulfide minerals. This late assemblage-related pyrite is optically homogenous and devoid of inclusions also, no evidence of deformation compared to early stage pyrite (Fig. 6a). Chalcopyrite is the second most abundant sulfide mineral, occurs as fine to very fine (50–200 μm) dispersed anhedral grains in quartzites (Fig.6a, b, and g). It occurs also as tiny inclusions intergrowing in the coarse-grained pyrite, or replacing early stage pyrite grains (Fig. 6f). Sphalerite, is usually cannot be observed as individual grains but, occurring typically as anhedral inclusions intergrown or filling the micro fractures in coarse-grained pyrite, (Fig. 6d and f). Sometimes in the large pyrite crystals, sphalerite inclusions are associated

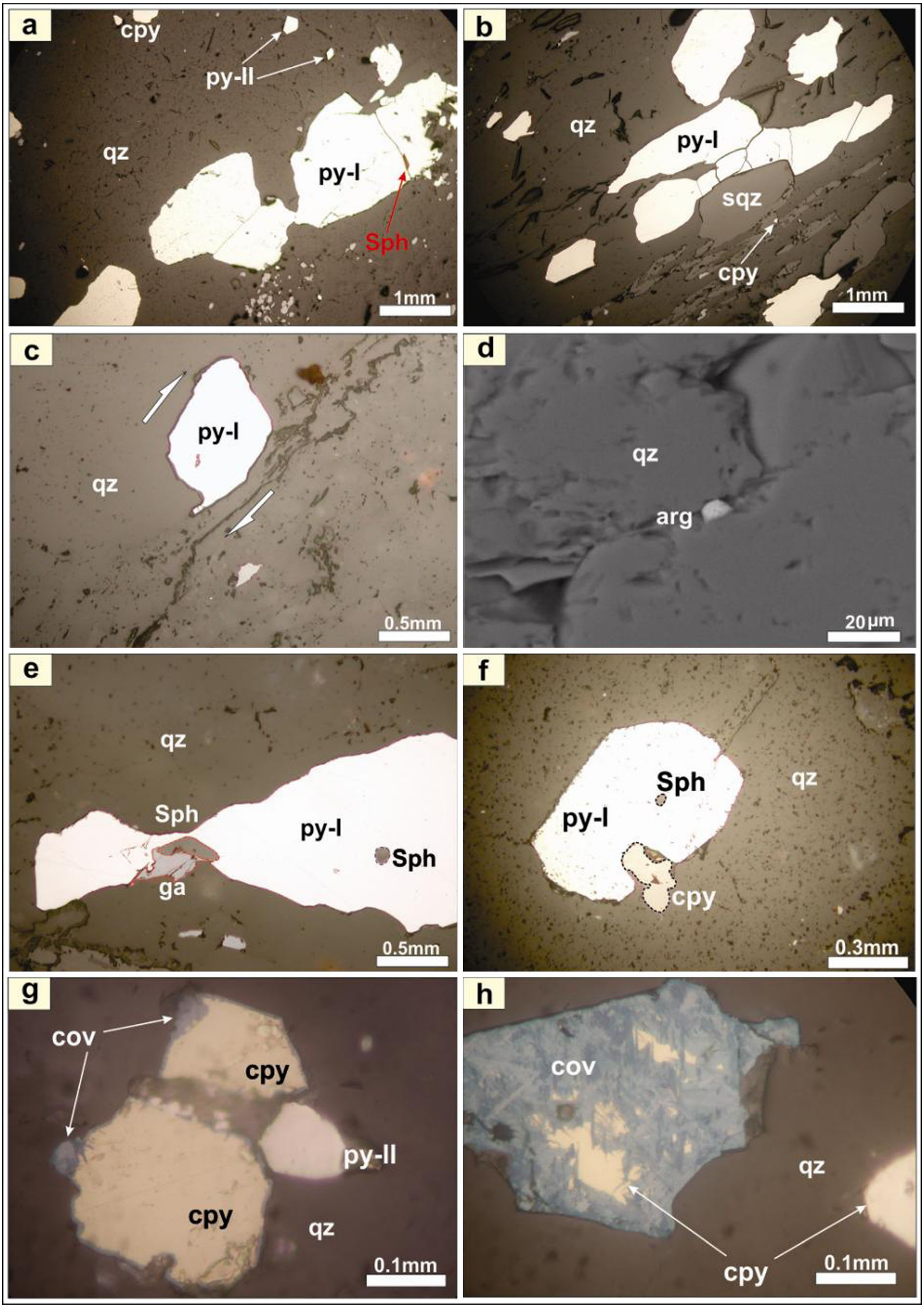
a
cpy
py-II
qz
py-I
Sph
1mm
b
qz
py-I
sqz
cpy
1mm
c
py-I
qz
0.5mm
d
qz
arg
20 μm
e
qz
Sph
py-I
Sph
ga
0.5mm
f
Sph
qz
py-I
cpy
0.3mm
g
cov
cpy
py-II
cpy
qz
0.1mm
h
cov
qz
cpy
0.1mm

◀ **Fig. 6** Photomicrographs of the ore minerals of GAH area mineralization. Abbreviations: *py-I* early phase pyrite, *py-II* late phase pyrite, *qz* quartz; *arg* silver, *cpy* chalcopyrite, *sph* sphalerite, *ga* galena. **a** Deformed pyrite (*py-I*) grains the fractures filled by sphalerite with disseminated pyrite (*py-II*) and chalcopyrite grains; **b** deformed pyrite (py-I) grains with fractures filled by sphalerite; **c** deformed pyrite (py-I) grain indicating right-lateral shear sense; **d** back-scattered electron images of silver inclusions in pyrite (py-I); **e** sphalerite and galena intergrown and inclusions with pyrite (py-I); **f** sphalerite intergrown with pyrite (py-I) and chalcopyrite replaces pyrite; **g** disseminated pyrite (py-II) and chalcopyrite with covelite replaces chalcopyrite along the grain boundaries; **h** Subhedral grains of chalcopyrite and covelite, where covelite replaces chalcopyrite

with galena (Fig. 6e). Covellite occurs as individual fine subhedral to anhedral grains (<300 μm). Covelite replaced some pyrite and chalcopyrite grains almost entirely (Fig. 6g and h).

Mineral paragenesis of GAH quartzite rocks have been determined according to the microscopic overgrowth and replacement textures displayed by the ore and gangue minerals. The concentration and textural relationships of the ore minerals do not change or modify significantly in the studied ore bodies, but generally can be discriminated as two mineralization phases. The early mineralization phase is represented by quartz, pyrite, pyrrhotite, argentite, and invisible gold. The later mineralization phase is manifested by quartz, muscovite, disseminated pyrite, galena, sphalerite, chalcopyrite, covellite, and±invisible gold.

Mode of occurrence of gold

The gold mineralization associated with base-metal sulfide minerals in GAH area is mostly occurred as invisible gold or submicrometer-size inclusions in pyrite. Based on the ore microscopic investigations, were distinguished two phases of pyrite, the pyrite (Py-I) related to early stage of the mineralization and another one (Py-II) related to late stage of the mineralization. Electron probe microanalysis (EPMA) (Table 2) of the two phases of pyrite reveal the presence of traces of As, Cu, and Ag in the first phase of pyrite (up to 0.03, 0.05, and 0.06, respectively); whereas these elements are much lower or not detected in the second phase of pyrite.

From EPMA analysis of pyrite whether early or late phase, most of trace elements as well as gold display very low to not detect concentrations because they are mostly below EPMA detection limits, so several pyrite grains have been separated from quartzites and analyzing by inductively coupled plasma mass spectrometry (ICP-MS) for trace elements in pyrite. Analysis by ICP-MS of early pyrite phase (Table 3) revealed the presence of trace amounts of Au (up to 8.33 ppm), Ag (up to 5.24 ppm), As (up to 6.48 ppm), Co (up to 52.82 ppm), Cu (up to 163 ppm), and Pb (up to 51.56 ppm). Au values positively correlate with As and Cu, while very weak or no correlation was observed between Au and other elements. On the other hand, Ag exhibits strong positive correlations with Co, Cu, Sr, and W (Table 4). The late stage pyrite also contains traces of Au (up to 1.47 ppm), and other elements show low concentration comparing to those of the early stage pyrite (Table 5). Au of the late stage also correlate positively with As, and no distinct correlation has been observed between Au and the other elements (Table 6).

Sulfur isotope

The sulfur isotope compositions of five pyrite separates (three early stage pyrite (Py-I) coarse-grained, and other two related to late stage pyrite (Py-II) fine-grained) hand-picked from powdered mineralized quartzites were examined. The $\delta^{34}S$ data frequency histogram (Fig. 7) shows that the early phase pyrite (Py-I) has values of −6.2, −7.9, and −8.6‰ and the late phase pyrite (Py-II) comprises two light $\delta^{34}S$ values of −10.4 and −12.1‰. Variations in the $\delta^{34}S$ values and clustering around two distinct categories can be attributed to different mineralization stages of the two pyrite phases. Sulfur isotope compositions for the two phases of pyrite suggesting an igneous source of sulfur, where sulfur with light $\delta^{34}S$ values (−12.1, −6.2) might have been derived directly from magmatic fluids (Ohmoto and Rye 1979).

Table 2 Representative EMPA data of two pyrite phases in quartzites

Wt%	Pyrite (I)									Pyrite (II)			
Fe	45.07	46.06	48.05	45.41	46.85	47.10	47.91	44.13	46.03	46.72	46.67	48.85	46.11
S	53.83	52.42	51.46	53.89	53.32	54.28	52.02	54.97	53.89	53.31	53.13	51.16	53.79
As	0.01	0.02	–	–	0.01	0.01	–	–	0.01	–	–	–	–
Cu	–	0.05	0.03	–	0.05	0.06	–	0.01	0.02	0.01	0.01	–	–
Ag	0.06	–	–	0.05	0.01	0.01	0.05	–	0.03	–	–	–	0.01
Au	–	–	–	–	–	–	–	–	–	–	–	–	–
Sum	99.06	98.57	99.57	99.37	100.28	101.47	100.00	99.17	100.03	100.04	99.81	100.02	99.90

"–" below detection limit

Table 3 ICP-MS trace element analysis of pyrite-I (all values are reported in ppm)

Sample	Py1	Py2	Py3	Py4	Py5	Py6	Py7	Py8	Py9	Py10
Au	8.33	2.41	1.98	0.29	0.15	0.90	7.43	3.98	6.62	2.70
As	6.48	1.26	1.19	0.85	1.17	1.36	4.38	3.58	3.47	2.78
Ag	0.90	0.67	5.24	0.25	0.89	0.65	1.11	0.18	0.17	0.14
Co	8.42	5.17	52.82	9.11	5.21	4.63	12.95	27.50	24.75	24.14
Cr	0.10	0.44	0.78	0.22	0.19	0.09	0.07	0.24	0.29	0.11
Cu	163	20.20	15.50	12.45	54.10	56.00	117.50	3.58	4.03	2.89
Ni	0.56	15.28	6.92	19.16	16.47	11.62	2.73	10.87	9.90	9.58
Pb	0.79	0.24	2.17	0.15	0.43	0.42	0.79	51.56	42.29	3.17
Sr	0.75	0.33	8.44	0.26	4.91	0.46	0.24	0.69	0.79	0.35
Ba	1.90	1.70	2.80	1.70	2.90	1.80	2.10	2.00	2.30	1.90
W	29.96	141.35	430.00	17.60	26.41	20.18	19.23	47.12	49.99	15.29

Discussion

Ore microscopic studies showed that pyrite, pyrrhotite, argentite, galena, sphalerite, chalcopyrite, and covelite are the main base-metal sulfide minerals associated with invisible gold mineralization. Pyrite is the most abundant ore mineral (>60 vol% of sulfide minerals) in the quartzites. Based on distinct chemical and textural features, two pyrite phases were identified in the mineralized quartzites. The early phase pyrite (Py-I) is synkinematic with the N–S striking shear zone (HSZ), that is characterized by uniformly high gold content, while the late phase pyrite (PyII) shows low gold concentration comparing to those of the early stage pyrite. The Cr–Ni–Co signature in some pyrite samples for both pyrite phases which reflects their crystallization is affected by surrounding mafic/ultramafic rock affinity and pronounced fluid–rock interaction. The generally light sulfur stable isotope values of both pyrite phases may suggest a magmatic source for sulfur (Ohmoto and Rye 1979). A systematic variation has been detected in δ^{34}S values from different pyrite stages. This observation may suggest that the two groups of pyrite (Py-I and PyII) are not a single mineralization phase and/or a heterogeneous ore fluid. This hypothesis can be supported by ore microscopy investigation, which reveals that the early phase pyrite (Py-I) occurs as large grain aggregates, with identifiable brittle–ductile deformation textures. However, the late phase pyrite (Py-II) occurs as disseminated small grains optically homogenous and no evidence of deformation has been observed comparing to those of the early stage pyrite.

According to Botros (2004), characterized sixteen gold and related sulfide deposits in the Eastern Desert of Egypt in which these deposits are obviously spatially and genetically related to brittle–ductile shear zones, mostly developed during late deformational stages among the evolution history of the Eastern Desert. Goldfarb et al. (2001) and Groves et al. (2003) reported that, orogenic gold as well as base-metal sulfide deposits are typically formed during late stages of the deformational metamorphic–magmatic history of the evolving orogeny, synkinematic with at least one main penetrative

Table 4 Correlation coefficient matrix of Au and trace elements in pyrite-I

	Au	As	Ag	Co	Cu	Ni	Sr	Ba	Pb	W
Au	1									
As	***0.927***	1								
Ag	−0.115	−0.219	1							
Co	0.053	−0.044	***0.701***	1						
Cu	***0.559***	−0.598	***0.735***	0.404	1					
Ni	−0.823	−0.818	−0.288	−0.283	0.259	1				
Sr	−0.326	−0.364	***0.872***	0.619	***0.702***	−0.022	1			
Ba	−0.127	−0.178	0.597	0.474	0.366	−0.062	***0.860***	1		
Pb	0.297	0.255	−0.274	0.336	−0.392	−0.006	−0.174	0.041	1	
W	−0.173	−0.323	***0.931***	***0.755***	0.675	−0.126	***0.802***	0.483	−0.111	1

Bold italicized values indicate significant positive correlation

Table 5 ICP-MS trace element analysis of pyrite-II and quartzites (all values are reported in ppm)

Pyrite-II										Quartzites				
Sample	Py11	Py12	Py13	Py14	Py15	Py17	Py18	Py19	Py20	Q10	Q11	Q13	Q14	Q17
Au	0.60	–	1.47	–	–	0.52	0.74	1.13	0.90	0.16	0.17	0.16	0.18	0.15
As	0.66	0.20	3.25	0.51	0.18	0.30	2.09	2.97	2.41					
Ag	0.17	0.31	0.54	0.44	0.66	0.60	0.11	0.13	0.15					
Co	5.51	57.65	10.7	44.99	32.29	39.44	27.29	24.39	29.1					
Cr	0.17	0.11	0.18	0.13	0.14	0.14	0.10	0.23	0.15					
Cu	113.5	15.10	35.9	9.65	6.78	9.34	2.22	3.01	3.00					
Ni	15.47	48.74	1.14	3.96	35.90	17.58	11.92	9.63	13.1					
Pb	0.81	0.09	1.19	0.28	0.36	0.38	3.67	2.62	554					
Sr	0.16	1.66	0.29	2.39	10.30	1.23	0.28	0.41	0.57					
Ba	1.80	1.80	2.40	2.00	4.20	1.80	1.80	2.00	1.90					
W	300	20.74	167	51.2	32.01	66.74	23.86	41.19	23.7					

Blank cells refer to unmeasured elements

"–" below detection limit

deformation stage of the host rocks. This observation is based on the occurrence of the deposits that cut across the deformational grains formed during orogenesis. As reported by Elsamani et al. (2001) gold mineralization in the Pan-African domains should be targeted near recognized sulfide concentrations, in collapse zones of extensional basins and along the shear zones that formed during the 650–550 Ma orogeny. The GAH area located at the extreme northern portion of the HSZ, this shear zone contains internal evidence of polyphase ductile shearing followed by brittle deformation (Almond and Ahmed 1987).

In GAH area structural controls are observed at different scales from a map-scale to a microscopic scale. The occurrence of the mineralized quartzites (host rock) within a NNW to N-trending map-scale shear zone (HSZ), represent the major control on mineralization distribution in the GAH area. Textures of open space filling are commonly absent, indicating that the fracture was invaded by highly pressured fluid followed by rapid precipitation (Coelho and Ramboz 1998). Moreover, the location where the shear zone traverses the lithotectonic contact between ophiolitic and metasediment rocks suggests that contrasting in the rock deformational state may have imparted sites for the ore fluids circulation (Zoheir 2008a, b, c). Inherited porosity, bends, and dilation formed by deflection of the host rock foliation into the shear zone have likely become act as physical trap and favorable sites for mineral precipitation. Analyses of the structural data collected from the quartzites and surroundings indicate the base-metal

Table 6 Correlation coefficient matrix of Au and trace elements in pyrite-II

	Au	As	Ag	Co	Cu	Ni	Sr	Ba	Pb	W
Au	1									
As	***0.916***	1								
Ag	−0.344	−0.492	1							
Co	−0.704	−0.540	0.212	1						
Cu	−0.012	−0.275	0.267	−0.485	1					
Ni	−0.650	−0.669	0.447	0.538	0.181	1				
Sr	−0.537	−0.419	0.324	0.226	−0.277	0.356	1			
Ba	−0.229	−0.136	0.305	−0.061	−0.223	0.187	***0.935***	1		
Pb	0.236	0.322	−0.315	−0.037	−0.229	−0.151	−0.140	−0.119	1	
W	0.290	0.028	−0.073	−0.737	***0.797***	−0.280	−0.274	−0.133	−0.220	1

Bold italicized values indicate significant positive correlation

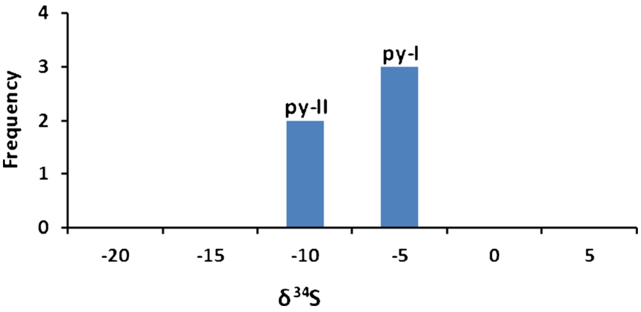

Fig. 7 Histogram of the distribution of $\delta^{34}S$ values of the two phases of pyrite (*py-I* and *py-II*) separated from mineralized quartzite rocks in GAH area

sulfide and associated gold mineralization in the GAH area is controlled by D3 transperssional deformation event. This event is main HSZ deformational event and characterized by transperssional stress regime, with σ1 trending E–W and σ3 trending N–S controlled NNW sinistral and NNE–SSW dextral strike slip faulting (Fig. 8). The parallelism of the magmatic foliation in granodiorite and the N–S (S3) mylonitic foliation related to this event in the HSZ shear zone suggests that the intrusion of the granodiorite and related hydrothermal solution is considered to have taken place during this deformation phase under brittle–ductile conditions.

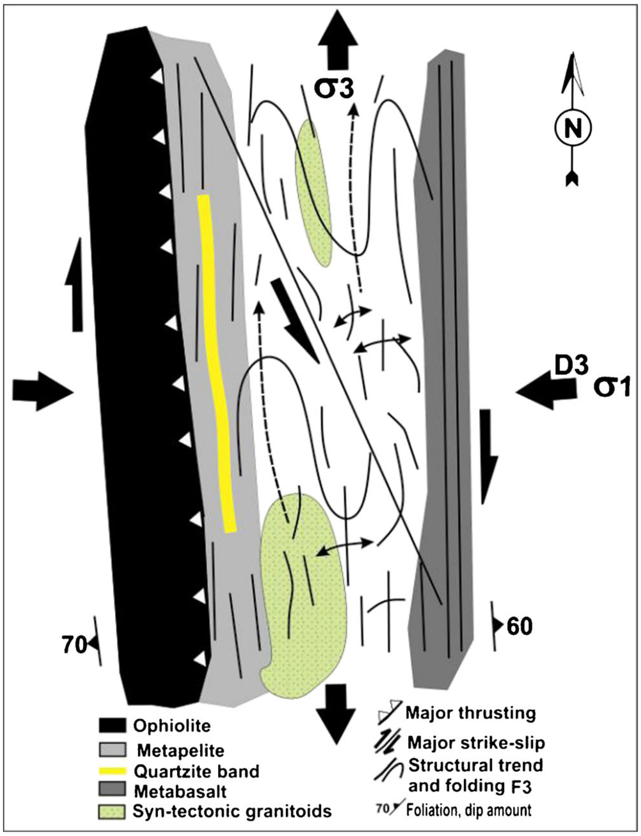

Fig. 8 Sketch map view of *D3*-deformational event that controlling base-metal sulfide and associated gold mineralization in the GAH area (not to scale)

Conclusions

Based on distinct chemical and textural data obtained from the microanalyses in the mineralized quartzites suggest the presence of at least two phases of sulfide minerals. The early mineralization phase includes pyrite (Py-I), pyrrhotite, argentite, and invisible gold, while the late phase, dominated by pyrite (Py-II), galena, sphalerite, chalcopyrite, covelite, and± invisible gold. The invisible gold is restricted to the two phases of pyrite, the early phase pyrite (Py-I) contains an average Au concentration 3.48 ppm with maximum value of 8.33 ppm, whereas the late phase pyrite (Py-II) contains an average Au concentration 0.60 ppm with maximum value of 1.47. Solid solution may be responsible for invisible gold in pyrite, whereas Chouinard et al. (2005) have reported that incorporation of gold into the structure of pyrite by coupled substitution of Au^{3+} with Cu^{+} ($Au^{3+}+Cu^{+}=2Fe^{2+}$), which requires unusually oxidizing conditions.

The base-metal sulfide and associated gold mineralization in the GAH area is mostly controlled by D3 deformational event (main HSZ deformation event). This event characterized by transperssional stress regime, with σ1 trending E–W and σ3 trending N–S, governed conjugate NNW sinistral and NNE–SSW dextral strike-slip faulting, likely during granodiorite emplacement. The geochronological framework established by Stern et al. (1990); Miller and Dixon (1992) indicates that the D3 occurred in the interval ~610–550 Ma late in the Neoproterozoic, which is manifested along the HSZ by upright folds and an apparent dextral offset. Accordingly, D3 and related mineralization should have taken place during the same period. The new structural, geochemical and mineralogical data presented in this contribution together with the detailed field investigation most likely indicate potential base-metal sulfide and associated gold ore bodies.

Acknowledgments This study was supported by the Japan MEXT Scholarship program (PhD scholarship to the first author) and Egyptian Nuclear Materials Authority (NMA). This project was financially supported by the Global Centre of Excellence (GCOE) program of Kyushu University, Japan. We are grateful to all members of the Abu Rushied project of the NMA for their assistance in the fieldwork. Many thanks to Dr. Jillian Gabo, Kyushu University for the improvement of the English phrasing.

References

Abdelsalam MG, Stern RJ (1996) Sutures and shear zones in the Arabian–Nubian Sheild. J Afr Earth Sci 23:289–310

Abdelsalam MG, Abdeen MM, Dowidar HM, Stern RJ, Abdelghaffar AA (2003) Structural evolution of the Neoproterozoic western Allaqi-Heiani suture zone, Southern Egypt. Precambr Res 124:87–104

Almond O, Ahmed F (1987) Ductilc shear zoncs on northern Red Sea Hills, Sudan and their implication for crustal collision. Geol J 22: 175–184

Botros NS (2004) A new classification of the gold deposits of Egypt. Ore Geol Rev 25:1–37

Burke K, Sengör C (1986) Tectonic escape in the evolution of the continental crust. AGU Geodynam Ser 14:41–53

Chouinard A, Paquette J, Williams-Jones E (2005) Crystallographic controls on trace element incorporation in auriferous pyrite from Pascua epithermal high-sulfidation deposit, Chile-Argentina. Can Mineral 43:951–963

Coelho CES, Ramboz C (1998) New interpretation on the genesis of the Fazenda Brasileiro and Fazenda Maria Preta gold deposits, Rio Itapicuru Greenstone Belt. Bahia, revista de Ouro Preto - REM 50(4):42–53

de Wall H, Greiling RO, Fouad Sadek M (2001) Post-collisional shortening in the late Pan-African Hamisana high strain zone, SE Egypt; field and magnetic fabric evidence. Precambrian Res 107:179–194

Elsamani Y, Almuslem A, El Tokhi M (2001) Geology and geotectonic classification of Pan-African gold mineralizations in the Red Sea Hills, Sudan. Int Geol Rev 43:1117e1128

Ghebreab W (1998) Tectonics of the Red Sea region reassessed. Earth Sci Rev 45:1–44

Goldfarb RJ, Groves DI, Gardoll S (2001) Orogenic gold and geologic time: a global synthesis. Ore Geol Rev 18:1–75

Groves DI, Goldfarb RJ, Robert F, Hart CJR (2003) Gold deposits in metamorphic belts: overview of current understanding, outstanding problems, future research, and exploration significance. Econ Geol 98:1e29

Gu XX, Liu MH, Zheng MH, Tang JX, Qi L (2002) Provenance and tectonic setting of the Proterozoic turbidites in Hunan, South China: geochemical evidence. J Sediment Res 72:393–407

Helmy HM, Kaindl R, Fritz H, Loizenbauer J (2004) The Sukari Gold Mine, Eastern Desert-Egypt: structural setting, mineralogy and fluid inclusion study. Mineral Deposita 39:495–511

Johnson PR, Woldehaimanot B (2003) Development of the Arabian-Nubian Shield: perspectives on accretion and deformation in the northern East African Orogen and the assembly of Gondwana. Geol Soc Lond Spec Publ 206:289–325

Johnson PR, Andresen A, Collins AS, Fowler AR, Fritz H, Ghebreab W, Kusky T, Stern RJ (2011) Late Cryogeniane Ediacaran history of the ArabianeNubian Shield: a review of depositional, plutonic, structural, and tectonic events in the closing stages of the northern East African Orogen. J Afr Earth Sci 61:167e232

Kröner A, Greiling RO, Reischmann T, Hussein IM, Stern RJ, Durr S, Kruger J, Zimmer M (1987) Pan African crustal evolution in northeast Africa. In: Kröner A (ed) Proterozoic lithospheric evolution, vol 17, American Geophysical Union, and Geodynamic Series., pp 235–257

Kröner A, Todt W, Hussein IM, Mansour M, Rashwan AA (1992) Dating of late Proterozoic ophiolites in Egypt and the Sudan using the single grain zircon evaporation technique. Precambr Res 59: 15–32

Kusky TM, Ramadan TM (2002) Structural controls on Neoproterozoic mineralization in the South Eastern Desert, Egypt: an integrated field, Landsat™, and SIR-C/X SAR approach. J Afr Earth Sci 35: 107–121

Kusky TM, Abdelsalam MG, Stern RJ, Tucker RD (2003) Evolution of East African and related orogens and the assembly of Gondwana (preface). Precam Res 123:81–85

Loizenbauer J, Neumayr P (1996) Structural controls on the formation of the Fawakhir gold mine, EL Sid-Eastern Desert, Egypt: tectonic and fluid inclusion evidence. Proceedings of the Geological Survey of Egypt Centennial Conference, pp 447–488

Miller MM, Dixon TH (1992) Late Proterozoic evolution of the N part of the Hamisana zone, northeast Sudan: constraints on Pan-African accretionary tectonics. J Geol Soc Lond 149: 743–750

Ohmoto H, Rye RO (1979) Isotopes of sulphur and carbon. In: Barnes HL (ed) Geochemistry of hydrothermal ore deposits, 2nd edn. Wiley-Interscience, New York, pp 509–567

Robinson BS, Kusakabe M (1975) Quantitative preparation of sulfur dioxide, for 34Sp2S analyses, from sulfides by combustion with cuprous oxide. Anal Chem 47:1179–81

Stern RJ (1994) Arc assembly and continental collision in the Neoproterozoic East African Orogen: implications for consolidation of Gondwanaland. Ann Rev Earth Planetary Sci 22: 319–351

Stern RJ, Kröner A, Manton WI, Reischmann T, Mansour M, Hussein IM (1989) Geochronology of the late Precambrian Hamisana shear zone, Red Sea Hills, Sudan and Egypt. J Geol Soc Lond 146: 1017–1029

Stern RJ, Nielsen KC, Best E, Sultan M, Arvidson RE, Kröner A (1990) Orientations of Late Precambrian sutures in the Arabian–Nubian shield. Geology 18:1103–1106

Zoheir BA (2008a) Structural controls, temperature–pressure conditions and fluid evolution of orogenic gold mineralisation in Egypt: a case study from the Betam gold mine, south Eastern Desert. Mineral Deposita 43:79–95

Zoheir BA (2008b) Structural controls, temperature-pressure conditions and fluid evolution of orogenic gold mineralisation in Egypt: a case study from the Betam gold mine, south Eastern Desert. Mineral Deposita 43:79e95

Zoheir BA (2008c) Characteristics and genesis of shear zone-related gold mineralization in Egypt: a case study from the Um El Tuyor mine, south Eastern Desert. Ore Geol Rev 34:445e470

Zoheir BA (2011) Transpressional zones in ophiolitic mélange terranes: potential exploration targets for gold in the South Eastern Desert, Egypt. J Geochem Explor 111:23–38